



NuSTAR AND XMM-NEWTON OBSERVATIONS OF THE HARD X-RAY SPECTRUM OF CENTAURUS A

F. FÜRST¹, C. MÜLLER^{2,3,4}, K. K. MADSEN¹, L. LANZ⁵, E. RIVERS¹, M. BRIGHTMAN¹, P. AREVALO⁶, M. BALOKOVIĆ¹, T. BEUCHERT^{3,4}, S. E. BOGGS⁷, F. E. CHRISTENSEN⁸, W. W. CRAIG^{7,9}, T. DAUSER⁴, D. FARRAH¹⁰, C. GRAEFE^{3,4}, C. J. HAILEY¹¹, F. A. HARRISON¹, M. KADLER³, A. KING¹², F. KRAUß^{3,4}, G. MADEJSKI¹², G. MATT¹³, A. MARINUCCI¹³, A. MARKOWITZ¹⁴, P. OGLE⁵, R. OJHA^{15,16,17}, R. ROTHSCHILD¹⁴, D. STERN¹⁸, D. J. WALTON¹, J. WILMS⁴, AND W. ZHANG¹⁵

¹ Cahill Center for Astronomy and Astrophysics, California Institute of Technology, Pasadena, CA 91125, USA

² Department of Astrophysics/IMAPP, Radboud University Nijmegen, 6500 GL, Nijmegen, The Netherlands

³ Lehrstuhl für Astronomie, Universität Würzburg, D-97074 Würzburg, Germany

⁴ Dr. Karl-Remeis-Sternwarte and ECAP, D-96049 Bamberg, Germany

⁵ Infrared Processing and Analysis Center, California Institute of Technology, Pasadena, CA 91125, USA

⁶ Instituto de Física y Astronomía, Facultad de Ciencias, Universidad de Valparaíso, Valparaíso, Chile

⁷ Space Sciences Laboratory, University of California, Berkeley, CA 94720, USA

⁸ DTU Space, National Space Institute, Technical University of Denmark, DK-2800 Lyngby, Denmark

⁹ Lawrence Livermore National Laboratory, Livermore, CA 94550, USA

¹⁰ Department of Physics, Virginia Tech, Blacksburg, VA 24061, USA

¹¹ Columbia Astrophysics Laboratory, Columbia University, New York, NY 10027, USA

¹² Kavli Institute for Particle Astrophysics and Cosmology, Stanford University, Menlo Park, CA 94025, USA

¹³ Dipartimento di Matematica e Fisica, Università degli Studi Roma Tre, I-00146 Roma, Italy

¹⁴ University of California, San Diego, CASS, La Jolla, CA 92093, USA

¹⁵ NASA Goddard Space Flight Center, Greenbelt, MD 20771, USA

¹⁶ University of Maryland, Baltimore County, Baltimore, MD 21250, USA

¹⁷ The Catholic University of America, Washington, DC 20064, USA

¹⁸ Jet Propulsion Laboratory, California Institute of Technology, Pasadena, CA 91109, USA

Received 2015 November 4; accepted 2016 January 23; published 2016 March 8

ABSTRACT

We present simultaneous *XMM-Newton* and *Nuclear Spectroscopic Telescope Array* (*NuSTAR*) observations spanning 3–78 keV of the nearest radio galaxy, Centaurus A (Cen A). The accretion geometry around the central engine in Cen A is still debated, and we investigate possible configurations using detailed X-ray spectral modeling. *NuSTAR* imaged the central region of Cen A with subarcminute resolution at X-ray energies above 10 keV for the first time, but found no evidence for an extended source or other off-nuclear point sources. The *XMM-Newton* and *NuSTAR* spectra agree well and can be described with an absorbed power law with a photon index $\Gamma = 1.815 \pm 0.005$ and a fluorescent Fe K α line in good agreement with literature values. The spectrum does not require a high-energy exponential rollover, with a constraint of $E_{\text{fold}} > 1$ MeV. A thermal Comptonization continuum describes the data well, with parameters that agree with values measured by *INTEGRAL*, in particular an electron temperature kT_e between ≈ 100 –300 keV and seed photon input temperatures between 5 and 50 eV. We do not find evidence for reflection or a broad iron line and put stringent upper limits of $R < 0.01$ on the reflection fraction and accretion disk illumination. We use archival *Chandra* data to estimate the contribution from diffuse emission, extra-nuclear point sources, and the outer X-ray jet to the observed *NuSTAR* and *XMM-Newton* X-ray spectra and find the contribution to be negligible. We discuss different scenarios for the physical origin of the observed hard X-ray spectrum and conclude that the inner disk is replaced by an advection-dominated accretion flow or that the X-rays are dominated by synchrotron self-Compton emission from the inner regions of the radio jet or a combination thereof.

Key words: galaxies: active – galaxies: individual (Centaurus A) – X-rays: galaxies

1. INTRODUCTION

At a distance of 3.8 Mpc (Harris et al. 2010), Centaurus A (Cen A, PKS 1322–428, NGC 5128) is the closest active galaxy exhibiting powerful jets. It hosts a supermassive black hole with a mass of $M \sim 5 \times 10^7 M_\odot$, as estimated from dynamical modeling of the gas disk surrounding the black hole (Neumayer et al. 2007). Cen A is bright across the electromagnetic spectrum and among the first identified extragalactic X-ray sources (Bowyer et al. 1970). In recent years, it has been detected up to γ -ray energies by *Fermi*/LAT (Abdo et al. 2010a, 2010b) and H.E.S.S. (Aharonian et al. 2009). Due to its proximity, it is an ideal laboratory in which to study the physics of active galactic nuclei (AGNs) including jet-launching mechanisms and coronal geometry (see Israel 1998, for an extensive review).

Cen A shows a complex structure, revealed at different wavelengths. Optical observations reveal a prominent dust band across the giant elliptical host galaxy NGC 5128, possibly indicating a merger event (e.g., Israel 1998). Powerful radio lobes are seen, extending almost perpendicular to this dust lane out to a projected size of 10° on the sky (corresponding to about 600 kpc at the distance of Cen A). It is classified as a proto-typical Fanaroff–Riley type I radio galaxy (FR I, Fanaroff & Riley 1974).

Jets are observed and resolved from the radio up to X-ray energies. High-resolution radio observations probe the jet in detail from subparsec to kiloparsec scales (e.g., Kraft et al. 2002; Hardcastle et al. 2003; Feain et al. 2011; Müller et al. 2014). The X-ray jet, extending about $2'$, shows a knotty substructure with spectral steepening to the jet edges (Hardcastle et al. 2003; Worrall et al. 2008). It is resolved down to

about 50 ly from the core, at which point it becomes invisible over the core emission even in *Chandra*.

The soft X-ray (0.1–7 keV) morphology of Cen A shows a very bright AGN, a fainter jet, and surrounding diffuse emission. The diffuse emission originates from the hot interstellar medium (ISM), which is measurable as a soft thermal component in the X-ray spectrum, as well as from off-nuclear point sources, mostly low-mass X-ray binaries (Kraft et al. 2003). Accretion takes place at very low Eddington fractions (<0.2%, Evans et al. 2004), allowing a classification as a low-luminosity radio galaxy.

The broad-band X-ray spectrum of Cen A is complex, consisting of several emission components, in particular a soft thermal plasma at low energies (0.1–2 keV), a power-law continuum, and strong absorption. Their origin is still unclear, including whether the hard X-ray spectrum solely originates from Comptonization in a thermal corona close to the core or also has a jet synchrotron self-Compton (SSC) component from the inner jet, unresolved in X-rays (e.g., Markowitz et al. 2007; Abdo et al. 2010b; Fukazawa et al. 2011; Müller et al. 2014). The location and structure of the absorbing material is also still uncertain, and partial covering models have been discussed (e.g., Evans et al. 2004; Markowitz et al. 2007; Fukazawa et al. 2011). Further, Cen A shows strong N_{H} variations with time indicating a clumpy torus (Rivers et al. 2011b; Rothschild et al. 2011; Markowitz et al. 2014).

The hard power-law continuum (\sim 3–100 keV) can be well described by a power law with a spectral index of $\Gamma \sim 1.8$ with an average unabsorbed flux of $\mathcal{F}_{20-100 \text{ keV}} \approx 6 \times 10^{-10} \text{ erg cm}^{-2} \text{ s}^{-1}$, attenuated by strong absorption (typical N_{H} values $> 10^{23} \text{ cm}^{-2}$) at energies below 10 keV (see, e.g., Mushotzky et al. 1978; Baity et al. 1981; Beckmann et al. 2011; Rothschild et al. 2011, and references therein). On top of the continuum a strong Fe K α line is present, with an equivalent width of typically $\sim 80 \text{ eV}$ (Markowitz et al. 2007; Fukazawa et al. 2011).

Fluorescent Fe K α lines are often a tell-tale sign of reflection off dense material in AGNs and are commonly observed (e.g., Singh et al. 2011). However, reflection off the accretion disk or optically thick torus also leads to the production of a Compton hump between 10 and 30 keV (Ross & Fabian 2005), the existence of which is debated in Cen A (Fukazawa et al. 2011; Rivers et al. 2011b, and references therein). Furthermore, the observed Fe K α line in Cen A is always narrow, ruling out an origin close to the central black hole.

Based on *Suzaku* data, Fukazawa et al. (2011) report the detection of reflection, i.e., a Compton hump, when introducing a second power-law component ($\Gamma < 1.6$) to describe the continuum. Using *Chandra* and *INTEGRAL*/SPI data, Burke et al. (2014) come to a similar conclusion. However, Beckmann et al. (2011), using all *INTEGRAL* instruments, do not find a significant reflection component as modeled by pexrav (Magdziarz & Zdziarski 1995) and set a 3σ upper limit of $R < 0.28$. Here, R is the reflection fraction, which is defined as 1 for reflection off an infinite disk, i.e., a reflector covering 2π of the sky as seen from the primary X-ray source. Applying a physically motivated Comptonization model (compPS, Poutanen & Svensson 1996), Beckmann et al. (2011) found weak evidence for reflection with $R = 0.12^{+0.08}_{-0.10}$, which is still consistent with no reflection at the 1.6σ level.

Rothschild et al. (2011) studied over 12 years of *Rossi X-ray Timing Explorer* (RXTE) data and found a very stable photon

Table 1
Observation Log Showing the Observation Number for Each Observatory as Well as the Exposure Time for Each Instrument

ObsID	MJD range	Instrument	Exp. Time (ks)
<i>NuSTAR</i>			
60001081002	56510.54–56511.67	FPMA FPMB	51.26 51.35
<i>XMM-Newton</i>			
0724060601	56511.53–56511.66	EPIC-pn MOS 1 MOS 2	7.29 10.50 10.49
<i>Chandra</i> (see Appendix)			
7797, 7798, 7799, 7800	54181.37–54207.63	ACIS-I	373.35
15295	56535.91–56536.01	ACIS-I	5.35

index $\Gamma = 1.822 \pm 0.004$, despite significant variation in the X-ray flux, and no evidence for reflection. They argued that the line was likely produced in a Compton-thin torus, thereby not producing a measurable Compton hump. These findings were confirmed by Rivers et al. (2011b), who set an upper limit of $R < 0.005$ on the reflection fraction using RXTE.

Evans et al. (2004) used *Chandra* and *XMM-Newton* data to study the soft X-ray spectrum of Cen A in detail. They used heavily piled-up *XMM-Newton* data of two different observations taken in 2001 and 2002 from which they excised the inner $20''$ to reduce pile-up. Additionally they added the diffuse emission as measured by *Chandra* to the *XMM-Newton* background to obtain a clear measurement of the core spectrum. They find that for an accurate description of the *XMM-Newton* spectrum two absorbed power-law components are required, with the primary one having a photon index of $\Gamma_1 = 1.74^{+0.11}_{-0.09}$ and an absorption column of $N_{\text{H},1} = (1.19 \pm 0.13) \times 10^{23} \text{ cm}^{-2}$. For the second power law, they fixed the photon index at $\Gamma_2 = 2$ and measured an absorption column of $N_{\text{H},2} = (3.6^{+2.2}_{-2.3}) \times 10^{22} \text{ cm}^{-2}$.

Here, we present simultaneous *Nuclear Spectroscopic Telescope Array* (NuSTAR, Harrison et al. 2013) and *XMM-Newton* (Jansen et al. 2001) observations taken in 2013 August to study the AGN core (see Table 1). *NuSTAR* is ideally suited to studying reflection spectra in AGNs since it covers the Fe K α line region and the Compton hump with one instrument. This allows us to investigate the accretion geometry and the physics of the central engine through detailed spectral modeling. We also use archival quasi-simultaneous *Chandra* data to study possible contamination from the diffuse and point-source emission.

The remainder of the paper is organized as follows: in Section 2 we give an overview of the data used and data reduction procedures. In Section 3 we present X-ray images and search for extended emission at high energies. In Section 4 we describe the spectral modeling, including the contribution from the diffuse emission. We discuss our findings in Section 5 and summarize the results in Section 6. We adopt a redshift of $z = 0.0018$ throughout the paper and give errors at the 90% confidence level for one parameter of interest unless otherwise noted. Data analysis was performed with the Interactive

Spectral Interpretation System v1.6.2-30 (ISIS; Houck & Denicola 2000).

2. OBSERVATIONS AND DATA REDUCTION

2.1. *NuSTAR*

NuSTAR consists of two independent grazing incidence telescopes, focusing X-rays between 3 and 78 keV on corresponding focal planes consisting of cadmium–zinc–telluride pixel detectors. *NuSTAR* provides unprecedented sensitivity and high spectral resolution at energies above 10 keV, ideally suited to studying the Compton reflection hump. The two focal planes are referred to as focal plane modules (FPM) A and B. *NuSTAR* data were extracted using the standard NUSTARDAS v1.3.1 software. Source spectra were taken from a 100'' radius region center on the J2000 coordinates. The background was extracted as far away from the source as possible, from a 120'' radius region. This approach induces small systematic uncertainties in the background, as the background is known to change over the field of view (Wik et al. 2014). However, Cen A is over a factor ~ 10 brighter than the background even at the highest energies, so that these uncertainties are negligible. *NuSTAR* data were binned to a signal-to-noise ratio (S/N) of 20 in the relevant energy range of 3–78 keV within ISIS.

The average count-rate during the observations was $\approx 18.5 \text{ cts s}^{-1}$ per module. Only very slight variability was evident, with the count-rate declining by about 5% over the observation. No changes in hardness were visible, so we use the time-averaged spectrum for the remainder of this paper.

2.2. *XMM-Newton*

XMM-Newton observed Cen A as part of the Tracking Active Galactic Nuclei with Austral Milliarcsecond Interferometry program (TANAMI), an ongoing multi-wavelength, multi-year monitoring program of southern AGNs (Ojha et al. 2010; Müller et al. 2014). We reduced the *XMM-Newton* data using the standard scientific analysis software version xmmsas_20141104_1833-14.0.0+. The EPIC-pn camera (Strüder et al. 2001) was operated in small window mode to alleviate pile-up, while the MOS cameras (Turner et al. 2001) were operated in full frame mode to obtain a measurement of the diffuse and jet components. A detailed analysis of the *XMM-Newton* data will be presented in a forthcoming publication (C. Müller et al. 2016, in preparation). Here we concentrate on the energy range $> 3 \text{ keV}$ for a direct comparison with the *NuSTAR* data and to avoid contamination from the soft X-ray emission from the thermal extended plasma and the off-nuclear point sources.

Even though EPIC-pn was operated in the small window mode, the count-rate of $\approx 30 \text{ cts s}^{-1}$ is enough to cause pile-up (see the *XMM-Newton* users' handbook issue 2.13).¹⁹ We therefore carefully analyzed extraction regions with different annuli and compared spectral shapes and the results from epatplot. We found that only negligible fractions of pile-up remain for an inner radius of 10''. We set the outer radius to 40'', the largest radius possible with the region fully on the chip, as the source was located close to the north–east border of

the chip. We rebinned the pn data to a S/N of 15 between 3 and 10 keV.

Having been operated in full window mode, MOS 1 and 2 were more significantly piled-up, and we excluded the inner 20'' to remove most pile-up effects. We set the outer radius to 100'' to be comparable to the *NuSTAR* extraction region and rebinned the spectra to an S/N of 11.5 between 3 and 9 keV to retain sufficient spectral resolution for line spectroscopy despite the lower effective area compared to pn. Within that annulus, no other point source is visible. A more detailed study of the jet spectrum including *Chandra* will be presented in a forthcoming publication (C. Graefe et al. 2016, in preparation).

All annuli were centered on the J2000 coordinates of Cen A. The *XMM-Newton* data were taken contemporaneously to *NuSTAR*, overlapping in the last part of the longer *NuSTAR* observation. The complete observation log is given in Table 1.

3. IMAGING

We show the *NuSTAR* image in the 3–78 keV energy band in the left panel of Figure 1, which is consistent with a point source. Even after careful deconvolution of the image, we find no evidence for a deviation from a point source. In particular, the outer jet is not visible in the *NuSTAR* data. This is mainly due to the broad point-spread function (PSF) of *NuSTAR* with a half-power diameter of 60'' (Madsen et al. 2015b). The PSF smears out the very bright core over most of the bright jet emission. When summing up the counts observed by *Chandra* in knots AX and BX, as described by Kraft et al. (2000), we would expect a count rate of $\approx 5 \times 10^{-3} \text{ counts s}^{-1} \text{ module}^{-1}$ in *NuSTAR*. However, we measure 0.75 counts $\text{s}^{-1} \text{ module}^{-1}$ in the jet region, i.e., almost two orders of magnitude larger. The counts in this region are completely dominated by the core emission and the Poissonian noise is of the same order as the expected jet count rate. *Chandra* analysis also indicates that the jet is mainly visible in the soft X-rays (C. Graefe et al. 2016, in preparation), making a detection above $> 3 \text{ keV}$ unlikely.

The right panel of Figure 1 shows the MOS 1 image together with the X-ray contours from *Chandra*. While the MOS PSF has a half-energy width of only 13'', the Cen A core is so bright that it contributes significantly to the image out to at least 110''. The spikes surrounding the core in the image are due to the X-ray optics. Cen A's jet extends to the northeast and can be made out in the MOS data. The diffuse emission as observed by *Chandra* is too weak to contribute visibly to the image. Note also that the off-nuclear point sources (e.g., in the southwest corner) are not visible in *NuSTAR*.

4. SPECTRAL MODELING

We modeled the *NuSTAR* FPMA and B and the *XMM-Newton* EPIC-pn, MOS 1, and MOS 2 data taken in 2013 August simultaneously with ISIS, allowing for cross-calibration constants between the instruments (CC_i). We give all fluxes relative to FPMA ($CC_{\text{FPMA}} = 1$). The *NuSTAR* and *XMM-Newton* data show big discrepancies between 3 and 5 keV, with *NuSTAR* measuring a significantly higher flux than the *XMM-Newton* instruments. This discrepancy has also been observed in other simultaneous data as well as with *Swift*/XRT and is at the time of writing being investigated by the *NuSTAR* team (K. K. Madsen et al. 2016, in preparation). We ignore *NuSTAR* data below 5 keV for now, as the *XMM-Newton* EPIC-pn data have a higher S/N (but see Section 4.2). We consequently use

¹⁹ http://xmm.esac.esa.int/external/xmm_user_support/documentation/uhb/index.html

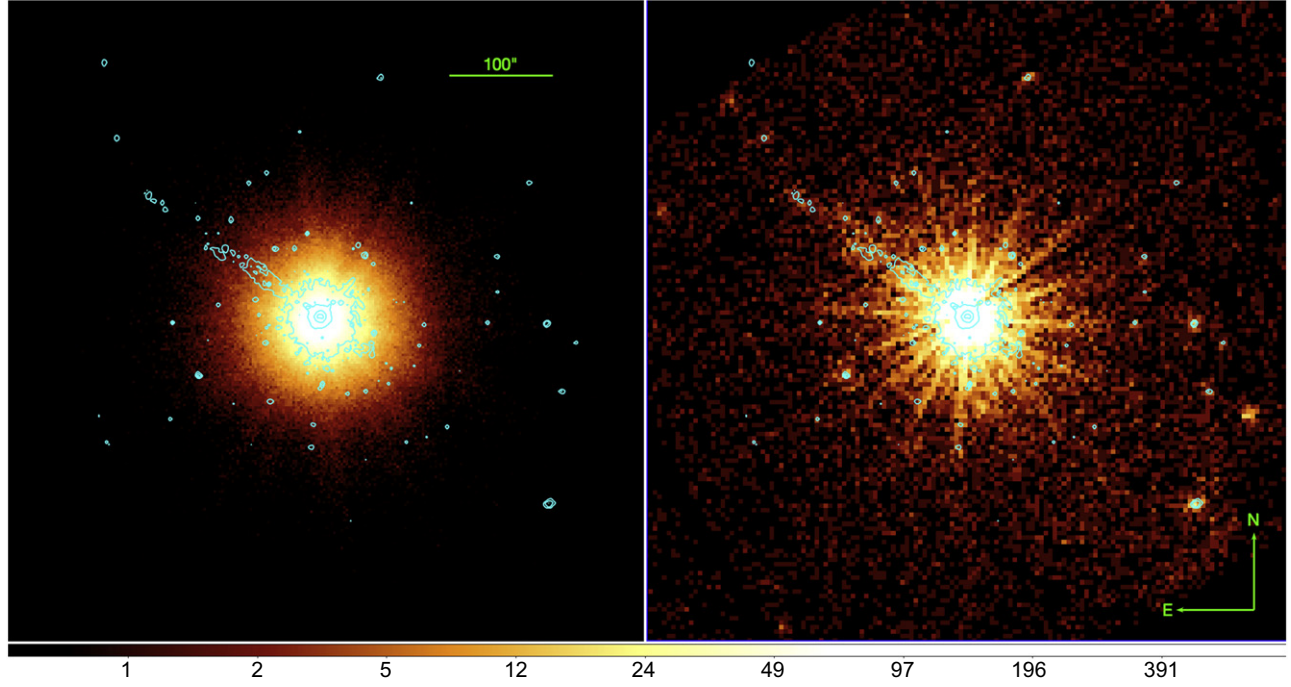


Figure 1. *NuSTAR* FPMA (left) and *XMM-Newton* MOS 1 (right) images of the Cen A core. North is up; east is to the left. Superimposed in cyan are the *Chandra* contours. The jet extends to the northeast and is faintly detected in the MOS image.

Table 2
Model Parameters for the Simultaneous *NuSTAR* and *XMM* Spectra

Parameter	Power Law	Cutoff-PL	pexrav	compPS	MYtorus	BNtorus
$N_H (10^{22} \text{ cm}^{-2})$	$17.06_{-0.24}^{+0.26}$	16.78 ± 0.26	$16.79_{-0.25}^{+0.26}$	$16.86_{-0.31}^{+0.30}$	$11.00_{-0.20}^{+1.53}$	$9.92_{-0.25}^{+0.14}$
$\mathcal{F}_{\text{cont}}^{\text{a}}$	0.9946 ± 0.0024	0.9896 ± 0.0024	0.9918 ± 0.0024	$0.9936_{-0.0024}^{+0.0028}$
Γ	1.815 ± 0.005	1.797 ± 0.005	1.797 ± 0.005	...	1.824 ± 0.006	$1.826_{-0.008}^{+0.009}$
$E_{\text{fold}} \text{ or } kT (\text{keV})$...	$(1.000_{-0.075}^{+0.000}) \times 10^3$	$(1.000_{-0.054}^{+0.000}) \times 10^3$	$(2.16_{-0.22}^{+0.19}) \times 10^2$
R	≤ 0.011	≤ 0.012
y	0.402 ± 0.016
$i [\text{deg}]$	60 (fix)	60 (fix)	>75.8	$63.30_{-0.11}^{+4.29}$
$\Theta_{\text{tor}} (\text{deg})$	60 (fix)	$60.00_{-2.97}^{+0.13}$
I_{Fe}^{b}	$(2.76 \pm 0.22) \times 10^{-4}$	$(2.88 \pm 0.22) \times 10^{-4}$	$(2.86 \pm 0.22) \times 10^{-4}$	$(3.38 \pm 0.26) \times 10^{-4}$
$E_{\text{Fe}} (\text{keV})$	$6.404_{-0.009}^{+0.005}$	$6.404_{-0.008}^{+0.004}$	$6.402_{-0.006}^{+0.007}$	$6.404_{-0.007}^{+0.004}$
$\sigma_{\text{Fe}} (\text{eV})$	≤ 8.7	≤ 8.8	≤ 8.5	≤ 8.7
CC_{FPMB}	1.0366 ± 0.0028	1.0366 ± 0.0028	$1.0366_{-0.0026}^{+0.0028}$	1.0366 ± 0.0028	1.032 ± 0.004	1.032 ± 0.004
CC_{pn}	0.848 ± 0.007	0.847 ± 0.007	0.847 ± 0.007	0.847 ± 0.007	0.866 ± 0.009	0.869 ± 0.009
CC_{MOS1}	1.214 ± 0.016	1.212 ± 0.016	1.212 ± 0.016	$1.213_{-0.014}^{+0.016}$	$1.109_{-0.018}^{+0.019}$	$1.116_{-0.018}^{+0.019}$
CC_{MOS2}	1.238 ± 0.016	1.236 ± 0.016	1.237 ± 0.016	$1.237_{-0.015}^{+0.016}$	1.128 ± 0.019	1.135 ± 0.019
χ^2/dof	1595.50/1532	1620.63/1531	1620.67/1530	1595.72/1531	1667.04/1536	1695.77/1535
χ^2_{red}	1.041	1.059	1.059	1.042	1.085	1.105

Notes.

^a Unabsorbed flux in $\text{keV s}^{-1} \text{cm}^{-2}$ [3–50 keV].

^b In $\text{ph s}^{-1} \text{cm}^{-2}$.

NuSTAR between 5 and 78 keV, *XMM-Newton* pn between 3 and 10 keV, and MOS between 3 and 9 keV.

4.1. Point-source Emission

We first fit the data with an absorbed power law as shown in Figure 2. A prominent Fe K α line is visible in the residuals (Figure 2(b)), which can be described with a narrow Gaussian around 6.4 keV with an equivalent width of ≈ 40 eV. The Gaussian is narrower than the energy resolution of *XMM-*

Newton and we only find upper limits for its width. The absorption is modeled with the phabs model, using abundances by Wilms et al. (2000) and cross-sections by Verner et al. (1996). This model gives a good fit ($\chi^2_{\text{red}} = 1.04$ for 1532 degrees of freedom (dof)) with a power-law index $\Gamma = 1.815 \pm 0.005$. We calculate an unabsorbed 3–50 keV luminosity of $\approx 3.4 \times 10^{42} \text{ erg s}^{-1}$. All parameters can be found in Table 2. Note that uncertainties are purely statistical and do not take systematic differences between the detectors

into account (e.g., the photon index can vary by ≈ 0.01 between consecutive observations in *NuSTAR* and the line energies have about 15 eV systematic uncertainties; see Madsen et al. 2015b).

To investigate the process responsible for the hard X-ray continuum and estimate the coronal temperature in a thermal Comptonization scenario, we searched for the presence of an exponential rollover at high energies by replacing the power law with the `cutoffpl` model in XSPEC. The fit did not improve and we obtained a lower limit of $E_{\text{fold}} > 1$ MeV (see Table 2). This limit is far above the *NuSTAR* energy range and therefore unreliable. However, as the `cutoffpl` is only a phenomenological model that shows continuous curvature even far below the folding energy, this result indicates that the 3–78 keV spectrum of Cen A is a pure power law.

For a more realistic description of a continuum produced by Comptonization, we applied the `compps` model (Poutanen & Svensson 1996). Following Beckmann et al. (2011), we assume a multi-colored disk with a slab geometry and fit for the Compton-y parameter. The disk input temperature cannot be constrained with our data due to obscuration, so in a first approach we fix it at $kT_{\text{BB}} = 10$ eV, appropriate for a black hole mass of $5 \times 10^7 M_{\odot}$ accreting at very low Eddington fractions (Makishima et al. 2000). The `compps` model also includes a reflection component based on the `pexrav` model and described by the reflection strength R , which we allow to vary. The inclination²⁰ was set to $i = 60^\circ$. To describe the Fe K α line, we added a Gaussian component and obtained a very good fit, with $\chi^2_{\text{red}} = 1.04$ for 1531 dof. The values obtained for $y = 0.402 \pm 0.016$ and the coronal temperature $kT_e = 216^{+19}_{-22}$ keV agree very well with the results from Beckmann et al. (2011); see Table 2. We only find an upper limit on the reflection strength at the 90% confidence level of $R \leq 0.012$.

We investigated the influence of the disk input temperature on other parameters within a reasonably expected range, sampling temperatures between $kT_{\text{BB}} = 5$ –50 eV. We find that the plasma temperature to first order decreases with hotter disk temperatures, from 277^{+21}_{-26} keV at 5 eV to 118^{+13}_{-14} keV at 50 eV. At higher input temperatures, however, a secondary minimum evolves at high plasma temperatures around 350 keV, which becomes statistically preferred above ~ 60 eV. At $kT_{\text{BB}} = 100$ eV we then measure an electron temperature of 304^{+19}_{-16} keV. We note that a disk temperature above 50 eV is likely too high for the parameters of Cen A’s black hole and we therefore do not investigate this solution further.

Using the `comptt` model (Titarchuk 1994) only gives a lower limit of $kT_e > 475$ keV. The measured value of the electron temperature should be taken with a grain of salt and is strongly influenced by our assumptions. A full investigation of the systematic uncertainties is, however, beyond the scope of this paper.

Despite the fact that electron temperature is above the energy range covered by *NuSTAR*, we can constrain kT_e for a given disk temperature due to the spectral shape and the high S/N of our data. In Figure 3 we show the χ^2 confidence contours for kT_e versus the Compton-y parameter, assuming $kT_{\text{BB}} = 10$ eV. While a clear degeneracy can be seen, both parameters are well constrained. When we directly fit for the optical depth τ instead of y , we find a very similar contour and a best-fit value of $\tau = 0.240^{+0.041}_{-0.027}$.

²⁰ Here $i = 0^\circ$ corresponds to a face-on view, while $i = 90^\circ$ corresponds to an edge-on view.

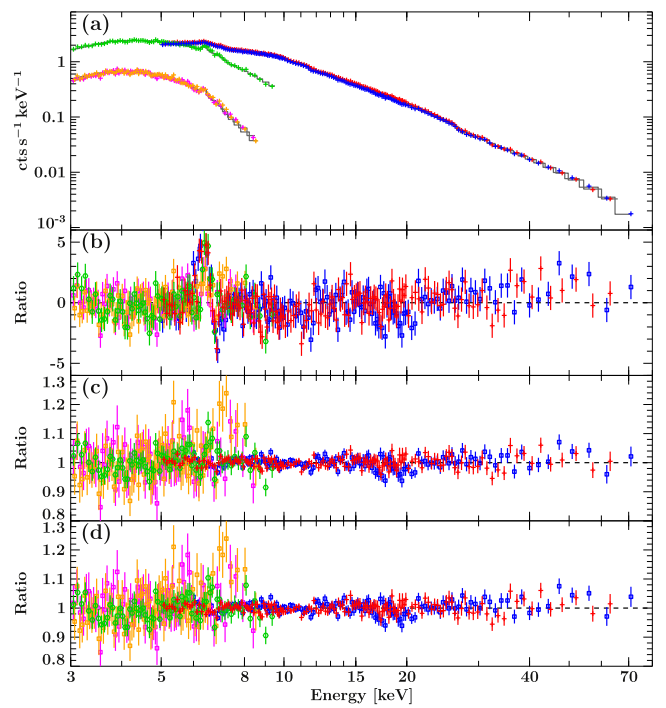


Figure 2. (a) *XMM-Newton* pn (green), MOS 1 (orange), and MOS 2 (magenta) as well as *NuSTAR* FPMA (red) and FPMB (blue) spectra. The best-fit power-law model with an additional Fe K α line is superimposed in gray. (b) Residuals in terms of χ for the best-fit power-law model without the Fe K α line (MOS 1 and 2 show similar residuals but are not shown for clarity). (c) Residuals in terms of ratio to the best-fit power-law model, including the Fe K α line. For details see the text. (d) Residuals for the best-fit `compps` model. Data were rebinned for visual clarity.

To test if the intrinsic shape of the `compps` is concealing any weak reflection component, we then modeled the spectrum using only the `pexrav` model. We note that the `pexrav` model does not make any assumptions about the geometry of the reflecting medium and is therefore also mostly a phenomenological model to test for the presence of curvature. Again, we only obtain an upper limit of $R \leq 0.010$ on the reflection fraction (Table 2). The value depends on the assumed inclination (here we used an inclination of $i = 60^\circ$ following Fukazawa et al. 2011) and is even lower for smaller angles (≈ 0.006 at the model maximum $\cos(i) = 0.95$). This limit is similar to the one obtained by Rivers et al. (2011b) using *RXTE* data ($R < 0.005$).

Models that self-consistently describe the reflection spectrum off an optically thick disk, like `pexmon` (Nandra et al. 2007), `reflionx` (Ross & Fabian 2007), and `xillver` (García & Kallman 2010), and include line fluorescence and a Compton hump, fail to provide an adequate description of the spectrum within physically sensible parameters. These models cannot combine the strength of the iron line with the lack of a Compton hump, indicating that the Fe K α line does not originate from reflection off Compton-thick material.

Finally, we tested physically motivated models for the presence of a toroidal obscuring structure in the nuclear region of Cen A. We applied the X-ray spectral models of Brightman & Nandra (2011, BNTorus) and Murphy & Yaqoob (2009, MYTorus), which were designed specifically for this purpose. The models self-consistently account for photoelectric absorption, fluorescence line emission (most importantly from Fe K α), and Compton scattering, assuming a toroidal

geometry. The MYTorus model assumes an obscuring torus with a circular cross-section and a fixed opening angle Θ_{tor} of 60° , while the BNTorus model assumes a spherical torus where N_{H} is independent of the inclination (i.e., viewing angle) i . The spherical torus is modified by a biconical void with a variable opening angle Θ_{tor} . Furthermore, BNTorus allows for variation of the covering factor of the torus, whereas MYTorus has a fixed covering factor of 0.5. For a recent comparison between these two models, see Brightman et al. (2015).

The BNTorus and MYTorus models measure similar line-of-sight column densities, $N_{\text{H}} = 9.92^{+0.13}_{-0.25} \times 10^{22} \text{ cm}^{-2}$ and $11.00^{+1.53}_{-0.20} \times 10^{22} \text{ cm}^{-2}$, respectively. The lower column densities compared to the previous models are due to the fact that the torus models also include Compton scattering, while phabs does not, which leads to an overestimation of the column in the latter. This is also reflected in the slightly lower unabsorbed 3–50 keV luminosity of the BNTorus model of $\approx 3.1 \times 10^{42} \text{ erg s}^{-1}$. The opening angle of the torus measured by BNTorus is $60.00^{+0.13}_{-2.97}$ degrees, which corresponds to a covering factor of 0.5. This covering factor compares well to other local AGNs of similar luminosity, such as NGC 1068, NGC 1320, and IC 2560 (Baloković et al. 2014; Bauer et al. 2015; Brightman et al. 2015).

For MYTorus, the inclination angle of the torus is derived to be $\geq 76^\circ$. MYTorus has the added flexibility of decoupling the scattered and fluorescent line components from the transmitted component in order to test for scattering out of the line of sight. However, when allowing for such a decoupling we only find marginal improvement in terms of χ^2 and the inclination angle becomes completely unconstrained. In that case we can place an upper limit of $1.15 \times 10^{23} \text{ cm}^{-2}$ on the N_{H} of any material out of the line of sight, consistent with what is seen along the line of sight.

Using *Suzaku* XIS and GSO data, Fukazawa et al. (2011) found a significant reflection fraction of the order of $R \approx 0.2$. Their best-fit model includes two power-law components describing the AGN core emission and the jet contribution separately. When applying their model to the *XMM-Newton* and *NuSTAR* data we cannot confirm such high reflection fractions but instead obtain upper limits on R similar to those in the simpler models presented in Table 2. Following Fukazawa et al. (2011) and using the pexmon model to self-consistently describe the Fe K α line and fixing the photon indices at 1.6 and 1.9, respectively, we obtain $R = 0.138 \pm 0.016$. However, the fit is clearly worse than the fits with only a single power law ($\chi^2_{\text{red}} = 1.16$ for 1531 dof).

We also investigated the presence of a partial covering model for the primary absorber, as used by, e.g., Evans et al. (2004). Because we only consider data above 3 keV, our limits are only marginally constraining, and we find a covering fraction > 0.98 . In Section 4.2 we extend the energy range down to 2 keV and find weak evidence for partial covering.

Using *Suzaku* data, Tombesi et al. (2014) found evidence for two weak absorption lines at 6.66 and 6.95 keV, which they interpreted as evidence for a slow wind. Similar absorption lines have recently been discovered in the *NuSTAR* spectrum of Cyg A, a bright FRII galaxy (Reynolds et al. 2015). When adding Gaussian absorption lines to our data of Cen A, with the energies fixed at the values found by Tombesi et al. (2014) and the width set to 1 eV, we find a marginal improvement of $\Delta\chi^2 = 7$ for two additional parameters. However, if we allow the energies to vary, the fit does not converge. The failure to

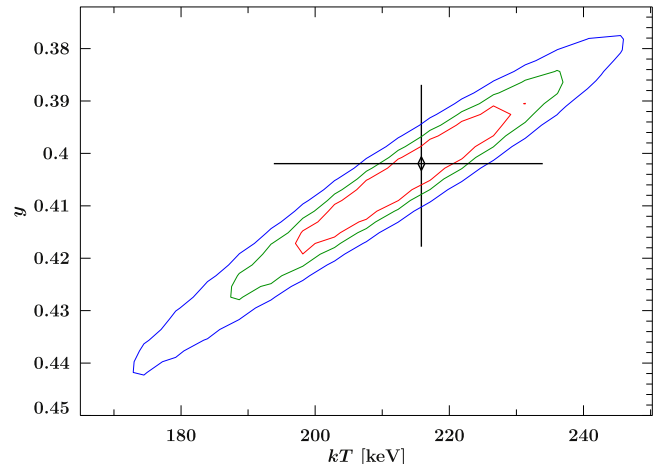


Figure 3. Contour map of the electron temperature kT_e vs. the Compton-y parameter in terms of χ^2 . The black cross indicates the best fit and its 90% uncertainties. The contours are given at the 1σ , 90%, and 99% confidence level (red, green, and blue, respectively).

detect significant absorption features could be due to the much lower S/N in the *XMM-Newton* data compared to the *Suzaku* data used by Tombesi et al. (2014). We therefore do not include these lines in our discussion.

4.2. Contribution from the Diffuse Emission

In the preceding section we attributed differences between the *XMM-Newton* and *NuSTAR* spectra to pile-up and cross-calibration differences. The strength of these effects required to explain the differences is, while not impossible, somewhat surprising. We therefore made an effort to rule out astrophysical or source intrinsic effects that could cause this discrepancy. The main source of intrinsic background contributing to the measured spectrum is diffuse emission surrounding the AGN as seen with *Chandra*. Due to the different PSF sizes of *XMM-Newton* and *NuSTAR*, the instruments sample different amounts of this diffuse emission, which might influence the observed spectral slope.

To check the influence of the diffuse emission as a function of distance to the AGN, we extracted spectra in different annuli from the *XMM-Newton* cameras. For the pn camera we use rings with $5''$ – $15''$, $15''$ – $25''$, and $25''$ – $40''$. We chose to avoid the central $5''$ to ensure the innermost pixel is excluded given pn's pixel size of $4''.1$. For MOS 1 and 2 we use annuli with $15''$ – $20''$, $20''$ – $40''$, $40''$ – $60''$, $60''$ – $80''$, and $80''$ – $100''$.

For *NuSTAR* we used an extraction region of $100''$, as described in Section 2.1. We also extracted spectra from smaller regions ($10''$ and $40''$) but did not find a significant difference in the spectral shape. We therefore chose to use the largest region for the best S/N.

We then fitted all these spectra simultaneously using a absorbed power law plus a Gaussian iron line. We required that all data have the same absorption column, photon index, and iron line energy, i.e., only allowed for the normalization of the continuum and the line to be different between the data sets. The iron line width was fixed to 10^{-6} keV, far below the energy resolution of any of the instruments.

When restricting the energy range to 5–78 keV for *NuSTAR* and 3–10 keV for *XMM-Newton*, we obtain a fit with values similar to those of the power-law fit in Table 2 (model A; see Table 3 in the Appendix), but with a worse statistical quality

Table 3
Model Parameters Using Simultaneous Fits of Different Annuli in *XMM*

Parameter	Model A ^a	Model B ^b	Model C ^c
N_{H} (10^{22} cm $^{-2}$)	17.63 ± 0.22	16.9 ± 0.4	17.8 ± 0.4
$A_{\text{cont}}^{\text{a}}$	0.2440 ± 0.0027	0.243 ± 0.006	0.253 ± 0.007
CF	...	$0.9932^{+0.0022}_{-0.0020}$	$0.9917^{+0.0021}_{-0.0020}$
Γ	$1.820^{+0.005}_{-0.004}$	1.831 ± 0.014	1.852 ± 0.015
E_{fold} (keV)	$(1.29^{+0.17}_{-0.14}) \times 10^2$
A_{Fe}^{a}	$(2.4 \pm 0.4) \times 10^{-4}$	$(2.4 \pm 0.4) \times 10^{-4}$	$(1.8 \pm 0.4) \times 10^{-4}$
E_{Fe} (keV)	$6.4500^{+0.0016}_{-0.0185}$	$6.408^{+0.004}_{-0.007}$	$6.407^{+0.005}_{-0.006}$
B_{FPM}	...	0.20 ± 0.09	1 (fix)
B_{pn} (5''–15'')	...	2.75 ± 0.29	$2.76^{+0.28}_{-0.30}$
B_{pn} (15''–25'')	...	0.5 ± 0.4	$1.36^{+0.29}_{-0.30}$
B_{pn} (25''–40'')	...	$0.10^{+0.12}_{-0.00}$	0.60 ± 0.26
B_{MOS} (15''–20'')	...	0.44 ± 0.22	0.48 ± 0.22
B_{MOS} (20''–40'')	...	0.93 ± 0.29	1.02 ± 0.29
B_{MOS} (40''–60'')	...	0.48 ± 0.20	0.53 ± 0.20
B_{MOS} (60''–80'')	...	0.87 ± 0.30	0.91 ± 0.30
B_{MOS} (80''–100'')	...	$1.0^{+0.9}_{-0.9}$	$1.0^{+0.9}_{-0.9}$
χ^2/dof	2356.72/1699	1989.06/1680	2081.68/1673
χ^2_{red}	1.387	1.184	1.244

Notes.

^a Model A: power law with measured background. *NuSTAR* is between 5 and 79 keV and *XMM* between 3 and 10 keV.

^b Model B: power law with additional diffuse background with free background scaling factor for all spectra. *NuSTAR* is between 5 and 79 keV and *XMM* between 2 and 10 keV.

^c Model C: cutoff power law with additional diffuse background where the background scaling factor for *NuSTAR*/FPMA is fixed at 1. *NuSTAR* is between 5 and 79 keV and *XMM* between 2 and 10 keV.

($\chi^2_{\text{red}} = 1.38$ for 1699 dof). When extending the energy range for *NuSTAR* down to 3 keV and for *XMM-Newton* down to 2 keV we do not find a statistically acceptable fit, even when allowing for a partial covering absorber ($\chi^2_{\text{red}} = 2.14$ for 1896 dof). Besides the clear mismatch of *NuSTAR* between 3 and 5 keV, the strongest residuals are due to the pn data, as shown in Figure 4. These data show different spectral slopes for different extraction region sizes, which might indicate spatial variation of the spectrum due to diffuse emission. This diffuse emission might also influence the *NuSTAR* spectrum between 3 and 5 keV and could be responsible for the observed discrepancies with *XMM-Newton*.

To investigate this we simulated how the diffuse emission, as seen with *Chandra*, influences the background in the different instruments and extraction regions. Details of the simulations are given in the Appendix. From these simulations it becomes clear that the diffuse emission cannot contribute enough flux to alter the observed *XMM-Newton* and *NuSTAR* spectra significantly. The core emission dominates over the diffuse background, even at large extraction radii. Even when allowing a scaling factor as a free parameter for each background, we do not obtain a good fit ($\chi^2_{\text{red}} = 1.24$ for 1673 dof) and the scaling factors reach unrealistic values (e.g., almost 3 for pn, i.e., the pn background needs to be three times higher than measured with *Chandra*).

We conclude from this investigation that the observed discrepancies between *NuSTAR* and *XMM-Newton* are attributed to pile-up and cross-calibration differences and that the diffuse emission around the AGN does not significantly influence the observed spectra. This result also implies that the measured data are completely dominated by the AGN itself and we obtain a clear view of the hard X-ray emission close to the central engine.

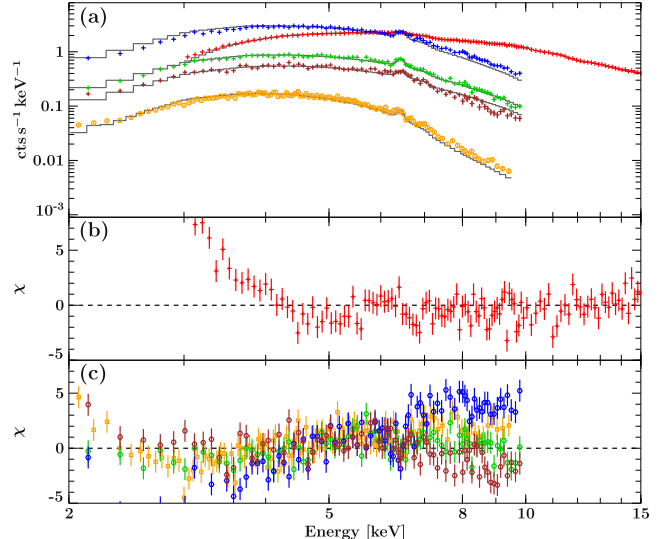


Figure 4. (a) Spectra and best-fit models in different annuli using the measured background and a partially absorbed power-law model. *NuSTAR* FPMA data are shown in red, *XMM-Newton* pn data between 5'' and 15'' in blue, between 15'' and 25'' in green, and between 25'' and 40'' in brown. For *XMM-Newton* MOS 1, residuals of all five annuli were combined into one spectrum for visual clarity, shown in orange. Data from *NuSTAR*/FPMB and *XMM-Newton*/MOS 2 are not shown for clarity. (b) Residuals in terms of χ for the *NuSTAR* data. (c) Residuals for the *XMM-Newton* data.

5. DISCUSSION

We used simultaneous *XMM-Newton* and *NuSTAR* data to measure the AGN emission of Cen A with the best S/N yet and to study the origin of the hard X-ray emission. We find that a simple absorbed power law or a thermal Comptonization

spectrum with an Fe K α emission line fits the 3–78 keV data very well. We do not find evidence for either an exponential rollover at high energies, a reflection component, or a partial covering absorber, and put stringent upper limits on the folding energy and reflection fraction (>1 MeV and <0.01 , respectively).

5.1. The Origin of the Iron Line

Many radio-loud AGNs that are not pure blazars, have a narrow Fe K α line with no indication of reflection from a disk close to the black hole and only weak evidence for distant reflection (e.g., 3C 33, Evans et al. 2010; 3C 382, Ballantyne et al. 2014; and 3C 273, Madsen et al. 2015a, see also Woźniak et al. 1998). The lack of relativistically blurred reflection has been discussed extensively in the literature, with the most common explanations being either an ionized inner accretion disk (Ballantyne et al. 2002), a slightly truncated inner accretion disk due to retrograde spin (Garofalo 2009), or an outflowing corona (Malzac et al. 2001, although their model predicts a significantly higher reflection strength for the measured photon index of Cen A). Weak and very weak reflection features are therefore not unusual in radio-loud AGNs like we find for the *NuSTAR* spectrum of Cen A.

The narrow Fe K α line likely originates from absorbing material relatively far away from the core. As shown by Rivers et al. (2011a), the absorber in Cen A is not Compton-thick, but is thick enough to produce the observed Fe K α line strength. In fact, assuming that a spherically symmetric absorbing medium surrounding the X-ray source is responsible for the observed Fe K α emission, the predicted equivalent width is much higher than observed. Following the calculations of Markowitz et al. (2007), for a measured column density of $N_{\text{H}} \approx 1.7 \times 10^{23} \text{ cm}^{-2}$ we obtain $\text{EW}_{\text{calc}} = 109 \text{ eV}$, compared to $\approx 40 \text{ eV}$ observed. As discussed by Markowitz et al. (2007) a spherically symmetric shell is a very simplified geometry, and if the absorber is only partially covering the X-ray source, the equivalent width will be reduced. Furthermore the calculation assumes solar abundances and the equivalent width can be significantly reduced with a sub-solar iron abundance.

A more realistic absorber geometry is a torus configuration, as invoked for many Compton-thick AGNs and as suggested from the unification scheme (see, e.g., Antonucci 1993). As demonstrated by Matt et al. (2003), column densities around $N_{\text{H}} \approx 10^{23} \text{ cm}^{-2}$ will lead to equivalent widths on the order of 40–50 eV, while not producing any significant Compton hump. As we have shown, physically motivated torus models (MYTorus, BNTorus) describe the data very well and self-consistently explain the strength of the iron line.

Infrared photometry of Cen A can also be well described with a (clumpy) torus model, with the caveat that the contribution of synchrotron emission to the IR data is not known (Ramos Almeida et al. 2009). From these IR models a column density around $N_{\text{H}} = 6.6_{-1.8}^{+2.2} \times 10^{23} \text{ cm}^{-2}$ for the torus is inferred, similar to the absorption column measured in the X-rays.

As shown by Rothschild et al. (2006), using *RXTE* data taken between 1996 and 2009 and comparing them to previous studies, the flux of the iron line is stable over long timescales (>10 year). We confirm these results and measure $I_{\text{Fe}} = (2.76 \pm 0.22) \times 10^{-4} \text{ ph cm}^{-2} \text{ s}^{-1}$. Similar values have been seen in *Suzaku*: $(2.3 \pm 0.1) \times 10^{-4} \text{ ph cm}^{-2} \text{ s}^{-1}$; Markowitz et al. 2007, and $[2.7\text{--}3.0] \times 10^{-4} \text{ ph cm}^{-2} \text{ s}^{-1}$; Fukazawa

et al. 2011), *BeppoSAX* ($2.7_{-1.4}^{+0.8} \times 10^{-4} \text{ ph cm}^{-2} \text{ s}^{-1}$; Grandi et al. 2003), and *XMM-Newton* ($\approx 2.4 \times 10^{-4} \text{ ph cm}^{-2} \text{ s}^{-1}$; Evans et al. 2004).

On the other hand, the continuum flux is strongly variable, by more than a factor of two (e.g., Rothschild et al. 2006). The flux presented here is about 40% higher than the average long-term flux observed by *INTEGRAL* (averaged over 6 years between 2003 and 2009; Beckmann et al. 2011). This results in a strong variability of the equivalent width of the iron line and limits the applicability of using the instantaneous X-ray flux to calculate the equivalent width. To explain the stability of the Fe K α flux, the fluorescent region needs to be on the order of 10 ly or more away from the core, to smear out its variations on that timescale. The region can still be much smaller than resolvable even with *Chandra* (as 1" is about 55 ly at the distance of Cen A).

5.2. Spectral Curvature at High Energies

Seyfert galaxies produce hard X-rays through thermal Comptonization of soft seed photons in a hot electron-gas corona. The temperature of the corona can be estimated from the energy of the exponential rollover, however, care has to be taken since the *cutoffpl* model has a distinctly different shape than calculations of a Comptonization spectrum (see, e.g., Petrucci et al. 2001). *NuSTAR* has measured folding energies in numerous Seyfert galaxies, e.g., IC 4329A (186 ± 14 keV; Brenneman et al. 2014), SWIFT J2127.4 +5654 (108 ± 11 keV; Marinucci et al. 2014), MCG-05-23-016 (116 ± 6 keV; Baloković et al. 2015), as well as determined lower limits in NGC 5506 with >350 keV and a best-fit ≈ 720 keV (Matt et al. 2015). Fabian et al. (2015) summarize and discuss these measurements. Recently, *NuSTAR* observations of the broad-line radio galaxy 3C 390.3 revealed a folding energy of 117_{-14}^{+18} keV (Lohfink et al. 2015), much lower than we find for Cen A. In Cen A the lower limit is in excess of 1 MeV, which, if the continuum is produced in a thermal corona, indicates a very high plasma temperature.

Following the calculations by Fabian et al. (2015) this very high temperature would put Cen A's corona far above the pair-production line for a coronal size of $10 r_g$. Only a corona orders of magnitude larger than typically measured for other AGNs would place Cen A in the physically allowed regime. However, the phenomenological nature of the *cutoffpl* model makes a physical interpretation difficult. A more realistic estimate of the temperature can be obtained using the thermal Comptonization *compps* model, which gives $kT_e = 216_{-22}^{+19}$ keV assuming a slab geometry and a seed photon temperature $kT_{\text{BB}} = 10$ eV. This temperature is stable against different geometries but depends on the seed photon temperature and spectral distribution. We find kT_e to be between 100 and 300 keV for input temperatures between 5 and 50 eV. Our results are consistent with the one measured by *INTEGRAL* for $kT_{\text{BB}} = 10$ eV but statistically better constrained ($kT_e = 206 \pm 62$ keV, Beckmann et al. 2011) and, assuming a slightly extended corona of $\sim 100 r_g$, are in line with the pair-production limit.

The value of the folding energy of Cen A is discussed extensively in the literature, with no clear consensus. For example, Rothschild et al. (2006) measure a folding energy >1.5 MeV using *RXTE* while at a similar luminosity, Kinzer et al. (1995) find $E_{\text{cut}} = 254 \pm 33$ keV using *CGRO/OSSE* data. From the fluxes and spectral shape measured between 0.2 and 30 GeV with *Fermi* it is clear that the spectrum needs to

roll over or break somewhere in the 100–1000 keV range (Abdo et al. 2010b).

It is interesting to note that nearly all well constrained measurements of a folding energy were performed by γ -ray instruments sensitive at energies >100 keV, while purely X-ray missions often find very high lower limits of the folding energy far outside their covered energy range. As discussed above, this effect is likely connected to the difference between a `cutoffpl` and a realistic Comptonization model: the `cutoffpl` model is constantly curving, even far below the folding energy, while a realistic Compton spectrum is much more power-law-like at energies significantly below the temperature of the Comptonization plasma and rolls over more steeply than the `cutoffpl` above it (see Figure 3 in Fabian et al. 2015 and references therein). γ -ray instruments like *INTEGRAL* therefore detect the cutoff, but given their typically lower statistics at soft X-rays find an acceptable solution with a `cutoffpl` or a broken power-law model (Kinzer et al. 1995; Beckmann et al. 2011). For the X-ray instruments, on the other hand, the rollover is outside their energy range and they mainly measure the power-law part of the Comptonization spectrum, resulting in unconstrained or very high folding energies when using `cutoffpl`. By using a more physical Compton spectrum we obtain a statistically well constrained measurement and show that a temperature between 100 and 300 keV is in line with the observed spectra. We note that the seed photon spectrum in an advection-dominated accretion flow (ADAF) is not necessarily described by a multi-temperature blackbody spectrum. However, by sampling a wide range of input temperatures we demonstrate that the measured cutoff depends only weakly on the exact seed photon spectrum.

5.3. The Geometry and Physics of the X-Ray Corona

Despite the exceptional quality of the *XMM-Newton* and *NuSTAR* data, the origin of the hard X-rays cannot be uniquely determined. Both models are consistent with the broad-band spectral energy distribution (SED) presented by Abdo et al. (2010b). To better constrain which emission mechanism is dominant in Cen A modeling, a simultaneous SED is necessary which will be presented in a forthcoming work (C. Müller et al. 2016, in preparation). We rule out any contribution from reflection from the inner accretion disk with high significance, similar to the X-ray spectra of other radio galaxies. This measurement is in line with the idea that the hard X-ray emission from Cen A is dominated by SSC emission from the inner radio jet (Mushotzky et al. 1978; Abdo et al. 2010b). In this model the X-rays are produced in an outflowing plasma by Compton up-scattering synchrotron seed photons, and it explains well the broad-band SED other than the TeV γ -ray flux detected by H.E.S.S. (Aharonian et al. 2009; Abdo et al. 2010b).

Beckmann et al. (2011) remark, however, that a jet origin of the hard X-rays is more difficult to reconcile with the small long-term variability of the X-ray flux, which is more reminiscent of Seyfert galaxies. A possible solution includes contribution from both components, a thermal corona as well as a synchrotron jet (Soldi et al. 2014). Such a combined model has been proposed for other radio galaxies as well, such as 3C 120 (Lohfink et al. 2014) and 3C 273 (Grandi & Palumbo 2004; Madsen et al. 2015a). However, as Rothschild et al. (2006) and later Burke et al. (2014) found, the X-ray continuum shape is remarkably stable over time, despite

significant flux changes. If the flux variability were induced by the inner jet component, we would expect some influence on the hard X-ray continuum. On the other hand, variability of the cutoff-energy as a function of flux has been observed with soft γ -ray instruments (e.g., with *CGRO*, Kinzer et al. 1995), following the “softer-when-brighter” correlation of Seyfert galaxies.

Some authors have reported a significant reflection fraction in Cen A (e.g., Fukazawa et al. 2011; Burke et al. 2014). If these detections are real, they do not seem to correlate with a particularly weak state of the X-ray flux, which we would expect if high fluxes correspond to a strong contribution from the jet emission, smearing out the reflection component. In particular, the *INTEGRAL*/SPI data used by Burke et al. (2014) are an average over 10 years, while Fukazawa et al. (2011) report a similar reflection fraction in both low and high flux states corresponding to a flux change of almost a factor of two. A mixture of standard thermal Comptonization and jet emission, in which the jet is driving the observed variability, thus seems unlikely.

If a stable accretion disk is present, we need to obscure it completely to eliminate all evidence of reflection from the observed spectrum. A puffed up accretion disk with a small corona could result in such an observed spectrum. However, Cen A is only accreting at $<0.2\%$ of its Eddington luminosity, making a geometrically thick accretion disk unlikely (Paltani et al. 1998). Rather, the accretion disk might be strongly truncated and replaced with an optically thin accretion flow, as in the advection-dominated accretion flow (ADAF) model (Narayan & Yi 1995).

Rieger & Aharonian (2009) propose that Cen A is dominated by ADAF emission, which they use to predict that Cen A might be a source of TeV photons and ultra-high-energy (UHE) cosmic rays. While the latter claim is disputed in the literature (Petropoulou et al. 2014, who instead favor a two-zone SSC model, with UHE particles emerging from the lobes, but see also Khiali et al. 2015 for a model using magnetic reconnection to produce γ -rays), a large ADAF can explain the observed hard X-ray properties. Typical temperatures for the electrons in an ADAF Comptonization plasma are on the order of 100 keV, in good agreement with our measurement.

The fact that the *NuSTAR* spectrum is rather simple and well described by one power law or Comptonization component also argues against a mix of X-ray sources and would instead seem to favor a common origin for all observed hard X-rays.

6. SUMMARY AND OUTLOOK

Using the exceptional quality of simultaneous *NuSTAR* and *XMM-Newton* spectra, we find that the core spectrum of Cen A can be described by a simple absorbed power law with a photon index $\Gamma \approx 1.8$ or a single-temperature Comptonization spectrum. The phenomenological `cutoffpl` does not provide a good fit and we argue that this is due to the fact that its shape does not represent a realistic Comptonization spectrum. From the Comptonization model, we find a coronal temperature of $kT_e \approx 220$ keV, for an assumed seed photon temperature of 10 eV.

We carefully analyzed the diffuse emission observed by *Chandra*, including the hot ISM, the outer jet, and off-nuclear point sources, and found that it does not significantly contribute to the observed hard X-ray spectrum from the core. The morphological and spectral analysis of the diffuse emission will

be presented in a forthcoming publication (C. Graefe et al. 2016, in preparation).

We put stringent upper limits on the contribution of Compton-thick reflection, with a reflection fraction $R < 0.01$. This rules out a standard Seyfert-like production of the hard X-rays and indicates that the inner accretion disk is replaced by optically thin gas. Despite the lack of reflection, the prominent iron line can be self-consistently described using a torus model, and we find inclinations marginally consistent with the torus being perpendicular to the jet-axis. We argue that Comptonization in an ADAF flow or at the base of the inner jet or both can explain the observed spectrum. Multi-epoch, multi-wavelength observations will help to disentangle the contribution from the jet and the ADAF and will be presented in a forthcoming publication (C. Müller et al. 2016, in preparation).

We thank the anonymous referee for comments that helped to improve this work. This work was supported under NASA Contract No. NNG08FD60C and made use of data from the *NuSTAR* mission, a project led by the California Institute of Technology, managed by the Jet Propulsion Laboratory, and funded by the National Aeronautics and Space Administration. We thank the *NuSTAR* Operations, Software, and Calibration teams for support with the execution and analysis of these observations. This research has made use of the *NuSTAR* Data Analysis Software (NuSTARDAS), jointly developed by the ASI Science Data Center (ASDC, Italy) and the California Institute of Technology (USA). Based on observations obtained with *XMM-Newton*, an ESA science mission with instruments and contributions directly funded by ESA Member States and NASA. This research has made use of a collection of ISIS scripts provided by the Dr. Karl Remeis Observatory, Bamberg, Germany at <http://www.sternwarte.uni-erlangen.de/isis/>. C.M. acknowledges the support of the Bundesministerium für Wirtschaft und Technologie (BMWi) through Deutsches Zentrum für Luft- und Raumfahrt (DLR) grant 50OR1404. We acknowledge support of the Deutsche Forschungsgemeinschaft (DFG) through grant Wi 1860 10-1. This research was funded in part by NASA through Fermi Guest Investigator grants NNN09ZDA001N, NNN10ZDA001N, NNN12ZDA001N, NNN13ZDA001N-FERMI. This research was supported by an appointment to the NASA Postdoctoral Program at the Goddard Space Flight Center, administered by Oak Ridge Associated Universities through a contract with NASA. M.B. acknowledges support from NASA Headquarters under the NASA Earth and Space Science Fellowship Program, grant NNX14AQ07H. We would like to thank John E. Davis for the `s1xfig` module, which was used to produce all figures in this work.

Facilities: *NuSTAR*, *XMM*, *CXO*.

APPENDIX

THE DIFFUSE EMISSION AS SEEN WITH *CHANDRA*

Cen A is known to show a complex morphology in X-rays as seen with *Einstein*, *ROSAT*, and *Chandra* (Feigelson et al. 1981; Turner et al. 1997; Kraft et al. 2000, 2002; Evans et al. 2004). In addition to an extended X-ray jet and point sources in the host galaxy, the AGN is surrounded by faint diffuse emission, extending about 1' (≈ 1 kpc) around the core. While this diffuse emission is not visible in the MOS image (Figure 1, right), it still might contribute to the observed X-ray spectrum. We therefore need to find a model for the extended emission,

which can be added to the modeling of the *XMM-Newton* and *NuSTAR* data. Such a model can only be obtained from *Chandra* due to its higher angular resolution. A detailed discussion of the *Chandra* data will be presented in a forthcoming publication (C. Graefe et al. 2016, in preparation), while here we only concentrate on its influence on the background.

Cen A has been observed multiple times by *Chandra* with both sets of CCDs of the Advanced CCD Imaging Spectrometer (ACIS; Weisskopf et al. 2000), but not simultaneous with *NuSTAR* and *XMM-Newton*. We selected a 5.34 ks ACIS-I observation (ObsID 15295; PI S. Murray) taken on 31 August 2013 which is in closest proximity to our *NuSTAR* observation. This observation, however, was too short to provide sufficient S/N to describe the diffuse spectrum accurately. We therefore looked through the archive for observations at a similar flux level and similar spectral shape and selected four of the longest ACIS-I exposures taken in 2007 (ObsID 7797-7800, PI: R. Kraft; see Table 1 for an overview of the data used.). We reprocessed each observation using CIAO version 4.5 to create new level 2 event files, following the software threads from the *Chandra* X-ray Center (CXC).²¹

We used the SPECEXTRACT task to extract X-ray spectra in each event file for several annular apertures centered on (13^h25^m27^s.59, -43^d01^m08^s.95) with radii of 5"-15", 15"-25", 25"-40", 40"-100", and 8"-100", i.e., matching the pn annuli. An exclusion aperture 3" wide was placed on each read-out streak, the direction of which varied with each exposure. The inner 5" were too piled-up for spectral extraction. A background spectrum was simultaneously extracted from the same chip in a sourceless region and automatically scaled based on the ratio of the source-to-background areas. We then combined the spectra from the four longest exposures for each annulus, using the COMBINE_SPECTRA task, which also calculates the combined background spectrum and response files. The spectra of the shallow, recent spectrum (ObsID 15295) shows little variation with respect to the deep, combined spectrum so that we base our analysis on the combined 2007 March data.

We fitted a partially covered power law to the data, requiring that all annuli have the same absorption column and covering fraction, but allowed for different photon indices and normalizations. This model is purely phenomenological and allows one to account for diffuse emission leaking at the lowest energies. We additionally added a narrow Fe K α line around 6.4 keV. The best-fit parameters for this model are given in Table 4. This model resulted in a very good fit, with $\chi^2_{\text{red}} = 1.05$ for 1630 dof. Adding an exponential rollover to the model by replacing the power law with the XSPEC `cutoffpl` model did not improve the fit and resulted in an unconstrained folding energy.

The core of Cen A is so strongly piled up that no events are registered at the center. Pile-up continues to be high out to $\approx 2''$. However, any diffuse emission in that region will also contribute to the diffuse background in *XMM-Newton* in the annuli outside of 3", as the PSF of *XMM-Newton* has a FWHM of about 4.5". We therefore try to estimate the contribution of the diffuse emission under the core by extrapolating the density profile of the *Chandra* image (using data from observation 7797 only). To do that, we construct the radial intensity profile centered at the core of Cen A by binning the events in a linear

²¹ <http://cxc.harvard.edu/ciao>

Table 4
Model Parameters for the *Chandra* Annuli Fits

Instrument	N_{H} (10^{22} cm^{-2})	CF	Γ	E_{Fe} (keV)	$I_{\text{cont}}^{\text{a}}$	I_{Fe}^{b}
ACIS 5-15	$25.6_{-2.0}^{+1.9}$	$0.841_{-0.011}^{+0.010}$	0.76 ± 0.09	$6.395_{-0.016}^{+0.015}$	$(5.9_{-1.0}^{+1.1}) \times 10^{-4}$	$1.21 \pm 0.18 \times 10^{-5}$
ACIS 15-25	1.09 ± 0.10	$6.429_{-0.030}^{+0.021}$	$(5.9_{-1.0}^{+1.2}) \times 10^{-4}$	$6.1 \pm 1.3 \times 10^{-6}$
ACIS 25-40	1.13 ± 0.10	$6.385_{-0.025}^{+0.026}$	$(5.7_{-1.0}^{+1.2}) \times 10^{-4}$	$6.5 \pm 1.3 \times 10^{-6}$
ACIS 40-100	1.61 ± 0.10	$6.409_{-0.030}^{+0.021}$	$(2.8_{-0.5}^{+0.6}) \times 10^{-3}$	$9.9 \pm 2.1 \times 10^{-6}$

Notes.^a In $\text{ph s}^{-1} \text{ cm}^{-2} \text{ keV}^{-1}$ at 1 keV.^b In $\text{ph s}^{-1} \text{ cm}^{-2}$.

grid with one pixel ($0.^{\prime\prime}492$) spacing as function of distance from the core. The profile is shown in Figure 5. The intensity drops dramatically inward of $2.^{\prime\prime}5$ due to the very high pile-up.

We describe this profile between $2.^{\prime\prime}4$ and $20.^{\prime\prime}$ with a broken power law plus a zero-centered Gaussian to estimate the contribution within the center. We set the break value of the broken power law to $1.^{\prime\prime}$ and the power-law index below that break to 0 to prevent the power law from rising to infinity at the center. Instead, the center is described by a Gaussian function with a width of $\sigma = 1.^{\prime\prime}63$. Using a β -model (Kraft et al. 2003) instead of a power law does not change the result, as at the relevant distances from the core the power-law part of the β -model dominates. We add another Gaussian line around $14.^{\prime\prime}3$ to describe the excess produced by a weak source. As can be seen in Figure 5, this model describes the radial profile very well. The exact rate of the center is not well constrained and we estimate our systematic uncertainties to be around a factor of 1.5–2.

Using this profile we fill in the piled-up region of the *Chandra* image, replacing the inner $5.^{\prime\prime}$ with counts drawn from a Poisson statistic as predicted by our model. This results in a very smooth image, shown in Figure 6. We use this spectrum as an input in simulating the contribution of the diffuse background in *XMM-Newton* and *NuSTAR*.

A.1. Diffuse Emission Simulation

The modified *Chandra* image shown in Figure 6 was used as input to the simulations and convolved with the respective *NuSTAR* and *XMM-Newton* PSFs. The extracted annuli were defined as regions with constant spectral properties, and each region was simulated into a separate image. When setting extraction regions for *NuSTAR* and *XMM-Newton*, we calculated the relative contributions of each image (or spectra) and folded the weighted input spectra through the response files and then combined them into the output spectrum for the requested region. These simulated spectra were then used as new background spectra for the *NuSTAR* and *XMM-Newton* data.

Because of the relatively modest extent of Cen A ($\approx 100.^{\prime\prime}$) and the scale of the extraction regions ($\approx 20.^{\prime\prime}$ – $40.^{\prime\prime}$), we made the following approximations to simplify the simulations: we assumed a flat effective area coinciding with the center of the object rather than a continuous extended effective area of the underlying diffuse component. This approximation is valid since most of the emission originates in the inner few arcseconds, dominating the response, and because at small off-axis angles ($< 2'$) the extended effective area of a circular region cancels out the area obtained from the center of a circle. In addition we did not include an energy-dependent PSF, since

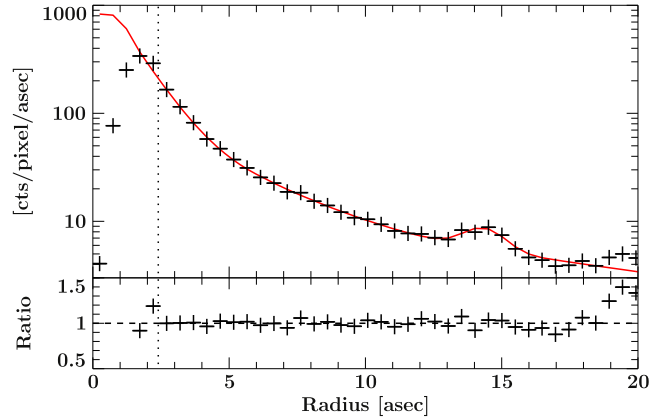


Figure 5. (a) Radial profile of the *Chandra* image of Cen A, binned into 1 pixel size bins ($0.^{\prime\prime}492$) as a function of distance from the core. The dotted line indicates $2.^{\prime\prime}5$, below which the data were ignored for the fit due to pile-up. The best-fit model is shown in red. The excesses at $\approx 14.^{\prime\prime}$ and $\approx 20.^{\prime\prime}$ are due to point sources. (b) Data-to-model ratio of the best fit.

the effect is typically on the order of a few arcseconds, while the scale size of our simulations was probing changes on a tens of arcseconds scale.

A.2. Results

We use the emission as estimated from the *Chandra* data as background for the different *XMM-Newton* annuli and the *NuSTAR* spectrum. We then fit the *XMM-Newton* and *NuSTAR* data between 2–10 keV and 3–78 keV, respectively, with a partially covered power law and an iron line simultaneously, allowing for the normalization of the continuum and the Fe K α line to change.

This additional background changes the fit parameters significantly (e.g., the photon index softens from $\Gamma = 1.82$ to $\Gamma \approx 1.95$), as the diffuse spectrum is very hard and we have no handle on a possible cutoff outside of *Chandra*'s energy range. This fit is statistically similar, with $\chi^2_{\text{red}} = 2.13$ for 1739 dof. The reduced number of degrees of freedom is due to our binning to a certain S/N level, which requires stronger binning for the now higher background. Allowing for a high-energy cutoff by replacing the power law with the `cutoffp1` model did not improve the fit significantly ($\chi^2_{\text{red}} = 2.02$ for 1738 dof) and gives a folding energy around $E_{\text{fold}} \approx 150$ keV.

A better fit can be achieved by allowing the normalization of the background to vary (model `recorn` in XSPEC), individually for each *XMM-Newton* and *NuSTAR* spectrum (while requiring FPMA and FPMB and each annulus of MOS 1 and 2 to have the same scaling factor). This approach significantly improved the fit to $\chi^2_{\text{red}} = 1.62$ for 1730 dof.

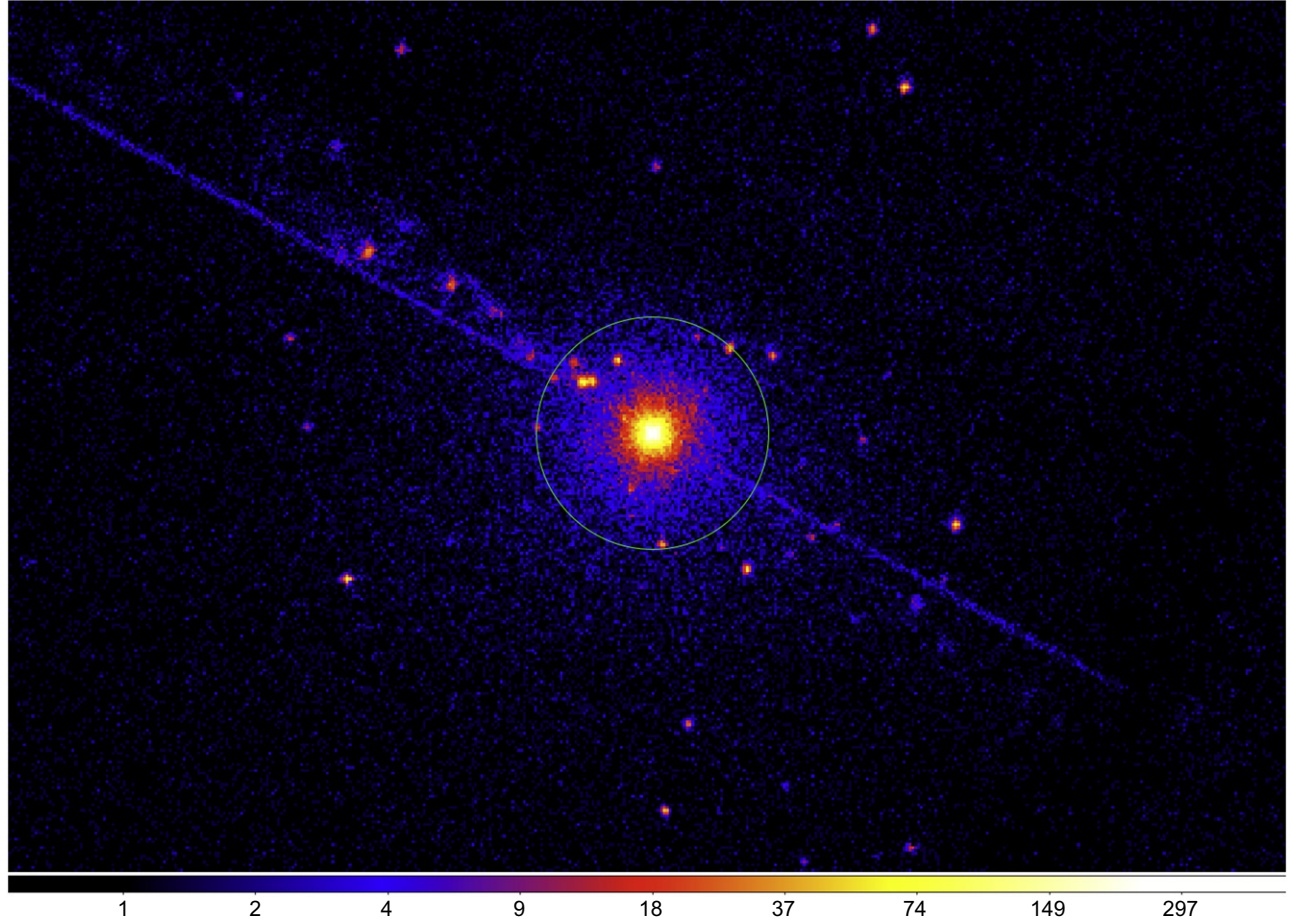


Figure 6. *Chandra* image of the Cen A core after filling in the piled-up core with or best estimate for the diffuse emission. North is up, east is to the left. The green circle is 20'' in radius.

However, strong residuals in the *NuSTAR* data below 5 keV are still present. We therefore rule out a significant contribution from the diffuse emission to the low-energy end of the *NuSTAR* spectrum.

By ignoring all *NuSTAR* data below 5 keV and allowing for a free scaling of the background we obtain a very good fit with $\chi^2_{\text{red}} = 1.18$ for 1680 dof (model B). However, the scaling factors are very widely spread with $\text{CB}_{\text{FPMA}} = 0.2$ and $\text{CB}_{\text{pn1}} = 2.5$, where pn1 denotes the factor for the innermost pn annulus between 5'' and 15''. We give the best-fit parameters in Table 3.

When forcing the scaling factor for *NuSTAR* to be 1, i.e., assuming that our simulations capture exactly the correct background, we only find an acceptable fit when at the same time allowing for an exponential high-energy rollover (using the cutoffpl model in XSPEC). This model gives $\chi^2_{\text{red}} = 1.25$ for 1675 dof (model C). The best-fit parameters are shown in Table 3. Still the scaling factors for the background of the other instruments vary wildly, indicating that the diffuse emission is not driving the observed differences.

REFERENCES

- Abdo, A. A., Ackermann, M., Ajello, M., et al. 2010a, *Sci*, 328, 725
 Abdo, A. A., Ackermann, M., Ajello, M., et al. 2010b, *ApJ*, 719, 1433
 Aharonian, F., Akhperjanian, A. G., Anton, G., et al. 2009, *ApJL*, 695, L40
 Antonucci, R. 1993, *ARA&A*, 31, 473
 Baity, W. A., Rothschild, R. E., Lingenfelter, R. E., et al. 1981, *ApJ*, 244, 429
 Ballantyne, D. R., Bollenbacher, J. M., Brenneman, L. W., et al. 2014, *ApJ*, 794, 62
 Ballantyne, D. R., Ross, R. R., & Fabian, A. C. 2002, *MNRAS*, 332, L45
 Baloković, M., Comastri, A., Harrison, F. A., et al. 2014, *ApJ*, 794, 111
 Baloković, M., Matt, G., Harrison, F. A., et al. 2015, *ApJ*, 800, 62
 Bauer, F. E., Arévalo, P., Walton, D. J., et al. 2015, *ApJ*, 812, 116
 Beckmann, V., Jean, P., Lubinski, P., Soldi, S., & Terrier, R. 2011, *A&A*, 531, A70
 Bowyer, C. S., Lampton, M., Mack, J., & de Mendonca, F. 1970, *ApJL*, 161, L1
 Brenneman, L. W., Madejski, G., Fuerst, F., et al. 2014, *ApJ*, 781, 83
 Brightman, M., Baloković, M., Stern, D., et al. 2015, *ApJ*, 805, 41
 Brightman, M., & Nandra, K. 2011, *MNRAS*, 413, 1206
 Burke, M. J., Jourdain, E., Roques, J.-P., & Evans, D. A. 2014, *ApJ*, 787, 50
 Evans, D. A., Kraft, R. P., Worrall, D. M., et al. 2004, *ApJ*, 612, 786
 Evans, D. A., Reeves, J. N., Hardcastle, M. J., et al. 2010, *ApJ*, 710, 859
 Fabian, A. C., Lohfink, A., Kara, E., et al. 2015, *MNRAS*, 451, 4375
 Fanaroff, B. L., & Riley, J. M. 1974, *MNRAS*, 167, 31
 Feain, I. J., Cornwell, T. J., Ekers, R. D., et al. 2011, *ApJ*, 740, 17
 Feigelson, E. D., Schreier, E. J., Delvaille, J. P., et al. 1981, *ApJ*, 251, 31
 Fukazawa, Y., Hiragi, K., Yamazaki, S., et al. 2011, *ApJ*, 743, 124
 García, J., & Kallman, T. R. 2010, *ApJ*, 718, 695
 Garofalo, D. 2009, *ApJ*, 699, 400
 Grandi, P., & Palumbo, G. G. C. 2004, *Sci*, 306, 998
 Grandi, P., Fiocchi, M., Perola, C. G., et al. 2003, *ApJ*, 593, 160
 Hardcastle, M. J., Worrall, D. M., Kraft, R. P., et al. 2003, *ApJ*, 593, 169
 Harris, G. L. H., Rejkuba, M., & Harris, W. E. 2010, *PASA*, 27, 457
 Harrison, F. A., Craig, W., Christensen, F., et al. 2013, *ApJ*, 770, 103
 Houck, J. C., & Denicola, L. A. 2000, in *Astronomical Data Analysis Software and Systems IX*, Vol. 216, ed. N. Manset, C. Veillet, & D. Crabtree (San Francisco, CA: ASP), 591
 Israel, F. P. 1998, *A&ARv*, 8, 237
 Jansen, F., Lumb, D., Altieri, B., et al. 2001, *A&A*, 365, 6
 Khiali, B., de Gouveia Dal Pino, E. M., & Sol, H. 2015, arXiv:1504.07592

- Kinzer, R. L., Johnson, W. N., Dermer, C. D., et al. 1995, *ApJ*, **449**, 105
 Kraft, R. P., Forman, W., Jones, C., et al. 2000, *ApJL*, **531**, L9
 Kraft, R. P., Forman, W. R., Jones, C., et al. 2002, *ApJ*, **569**, 54
 Kraft, R. P., Vázquez, S. E., Forman, W. R., et al. 2003, *ApJ*, **592**, 129
 Lohfink, A. M., Ogle, P., Tombesi, F., et al. 2015, *ApJ*, **814**, 24
 Lohfink, A. M., Reynolds, C. S., Vasudevan, R., Mushotzky, R. F., & Miller, N. A. 2014, *ApJ*, **788**, 10
 Madsen, K. K., Fürst, F., Walton, D. J., et al. 2015a, *ApJ*, **812**, 14
 Madsen, K. K., Harrison, F. A., Markwardt, C. B., et al. 2015b, *ApJS*, **220**, 8
 Magdziarz, P., & Zdziarski, A. A. 1995, *MNRAS*, **273**, 837
 Makishima, K., Kubota, A., Mizuno, T., et al. 2000, *ApJ*, **535**, 632
 Malzac, J., Beloborodov, A. M., & Poutanen, J. 2001, *MNRAS*, **326**, 417
 Marinucci, A., Matt, G., Kara, E., et al. 2014, *MNRAS*, **440**, 2347
 Markowitz, A., Takahashi, T., Watanabe, S., et al. 2007, *ApJ*, **665**, 209
 Markowitz, A. G., Krumpe, M., & Nikutta, R. 2014, *MNRAS*, **439**, 1403
 Matt, G., Guainazzi, M., & Maiolino, R. 2003, *MNRAS*, **342**, 422
 Matt, G., Baloković, M., Marinucci, A., et al. 2015, *MNRAS*, **447**, 3029
 Müller, C., Kadler, M., Ojha, R., et al. 2014, *A&A*, **569**, A115
 Murphy, K. D., & Yaqoob, T. 2009, *MNRAS*, **397**, 1549
 Mushotzky, R. F., Serlemitsos, P. J., Boldt, E. A., Holt, S. S., & Becker, R. H. 1978, *ApJ*, **220**, 790
 Nandra, K., O'Neill, P. M., George, I. M., & Reeves, J. N. 2007, *MNRAS*, **382**, 194
 Narayan, R., & Yi, I. 1995, *ApJ*, **452**, 710
 Neumayer, N., Cappellari, M., Reunanen, J., et al. 2007, *ApJ*, **671**, 1329
 Ojha, R., Kadler, M., Böck, M., et al. 2010, *A&A*, **519**, A45
 Paltani, S., Courvoisier, T. J.-L., & Walter, R. 1998, *A&A*, **340**, 47
 Petropoulou, M., Lefa, E., Dimitrakoudis, S., & Mastichiadis, A. 2014, *A&A*, **562**, A12
 Petrucci, P. O., Haardt, F., Maraschi, L., et al. 2001, *ApJ*, **556**, 716
 Poutanen, J., & Svensson, R. 1996, *ApJ*, **470**, 249
 Ramos Almeida, C., Levenson, N. A., Rodríguez Espinosa, J. M., et al. 2009, *ApJ*, **702**, 1127
 Reynolds, C. S., Lohfink, A. M., Ogle, P. M., et al. 2015, *ApJ*, **808**, 154
 Rieger, F. M., & Aharonian, F. A. 2009, *A&A*, **506**, L41
 Rivers, E., Markowitz, A., & Rothschild, R. 2011a, *ApJL*, **742**, L29
 Rivers, E., Markowitz, A., & Rothschild, R. 2011b, *ApJS*, **193**, 3
 Ross, R. R., & Fabian, A. C. 2005, *MNRAS*, **358**, 211
 Ross, R. R., & Fabian, A. C. 2007, *MNRAS*, **381**, 1697
 Rothschild, R. E., Markowitz, A., Rivers, E., et al. 2011, *ApJ*, **733**, 23
 Rothschild, R. E., Wilms, J., Tomsick, J., et al. 2006, *ApJ*, **641**, 801
 Singh, V., Shastri, P., & Risaliti, G. 2011, *A&A*, **533**, A128
 Soldi, S., Beckmann, V., Baumgartner, W. H., et al. 2014, *A&A*, **563**, A57
 Strüder, L., Briel, U., Dennerl, K., et al. 2001, *A&A*, **365**, L18
 Titarchuk, L. 1994, *ApJ*, **434**, 570
 Tombesi, F., Tazaki, F., Mushotzky, R. F., et al. 2014, *MNRAS*, **443**, 2154
 Turner, M. J. L., Abbey, A., Arnaud, M., et al. 2001, *A&A*, **365**, L27
 Turner, T. J., George, I. M., Mushotzky, R. F., & Nandra, K. 1997, *ApJ*, **475**, 118
 Verner, D. A., Ferland, G. J., Korista, K. T., & Yakovlev, D. G. 1996, *ApJ*, **465**, 487
 Weisskopf, M. C., Tananbaum, H. D., Van Speybroeck, L. P., & O'Dell, S. L. 2000, *Proc. SPIE*, **4012**, 2
 Wik, D. R., Hornstrup, A., Molendi, S., et al. 2014, *ApJ*, **792**, 48
 Wilms, J., Allen, A., & McCray, R. 2000, *ApJ*, **542**, 914
 Worrall, D. M., Birkinshaw, M., Kraft, R. P., et al. 2008, *ApJL*, **673**, L135
 Woźniak, P. R., Zdziarski, A. A., Smith, D., Madejski, G. M., & Johnson, W. N. 1998, *MNRAS*, **299**, 449